Ultramicroscopy 240 (2022) 113579

Contents lists available at ScienceDirect

Ultramicroscopy

journal homepage: www.elsevier.com/locate/ultramic

The effect of secondary electrons on radiolysis as observed by in liquid TEM: The role of window material and electrical bias

Lindsey A. Bultema [a], Robert Bücker [b], Eike C. Schulz [a,c], Friedjof Tellkamp [a], Josef Gonschior [a], R.J. Dwayne Miller [d,*], Günther H. Kassier [a,1,*]

[a] Max Planck Institute for the Structure and Dynamics of Matter, Hamburg, Germany
[b] Centre for Structural Systems Biology, Department of Chemistry, University of Hamburg, Notkestrasse 85, 22607 Hamburg, Germany
[c] Universität Hamburg, HARBOR, Luruper Chaussee 149, 22761 Hamburg, Germany
[d] Departments of Chemistry and Physics, University of Toronto, Toronto, Canada

ARTICLE INFO

Keywords:
Liquid TEM
Au nanoparticle growth
Secondary electrons
Formvar
Carbon
Si_3N_4

ABSTRACT

The effect of window material on electron beam induced phenomena in liquid phase electron microscopy (LPEM) is an interesting yet under-explored subject. We have studied the differences of electron beam induced gold nanoparticle (AuNP) growth subject to three encapsulation materials: Silicon Nitride (Si_3N_4), carbon and formvar. We find Si_3N_4 liquid cells (LCs) to result in significantly higher AuNP growth yield as compared to LCs employing the other two materials. In all cases, an electrical bias of the entire LC structures significantly affected particle growth. We demonstrate an inverse correlation of the AuNP growth rate with secondary electron (SE) emission from the windows. We attribute these differences at least in part to variations in SE emission dynamics, which is seen as a combination of material and bias dependent SE escape flux (SEEF) and SE return flux (SERF). Furthermore, our model predictions qualitatively match electrochemistry expectations.

1. Introduction

Liquid phase electron microscopy (LPEM) is a rapidly developing technique capable of nm and even Å scale resolution of *in-situ* physical, chemical or biological structures and processes [1–3]. While limitations to contrast and resolution in LPEM have remained a major discussion point ever since the inception of the technique [4,5], approaches towards improving imaging conditions are continually developed [6–8]. Recent theoretical work by de Jonge has provided guidelines to match samples to the most appropriate imaging methods and to optimize the relevant electron dose requirements [9]. The latter is crucial, as the success of most LPEM experiments demands a trade-off between desired spatial resolution and unwanted beam effects through excessive dose [10]. Radiolysis of water is a primary driving force of such effects, particularly in samples where solution chemistry or biological systems are being studied [3,11–14]. Seminal work by Schneider et al. quantitatively described the radiochemistry of water as applied to LPEM systems, with special focus on electron dose rate, lateral liquid cell geometry, and solution pH [15]. The action of graphene as a sacrificial radical scavenger, protecting organic species from oxidative damage in LPEM imaging, has been demonstrated by Cho et al. [16]. This was corroborated by Keskin and de Jonge, who found that microtubules suffer less structural degradation in the few nm spatial resolution regime when imaged in graphene LC's as compared to cryogenic preparation [17]. This and other work by Yuk et al. and Wang et al. indicate graphene has advantages over conventional Si_3N_4 as a choice for liquid cell (LC) window material [18,19].

Fundamental considerations, however, suggest that the role of LC window material on radiolytic products should extend beyond their potential action as sacrificial radical scavengers. Hydrated (aqueous) electrons (e^-_{aq}) are known to be one of the most reactive and important radiolytic species formed by ionizing radiation in water through the process of secondary electron (SE) generation [20]. With SEs as precursors of e^-_{aq}, the generation and dynamics of the former will play an important role in the radiochemistry occurring in a LC [21]. SEs are the lowest energy electrons excited by the primary electron (PE) beam that still have sufficient energy to overcome the material work function and thus capable of escaping into the vacuum. The typical emitted SE energy

* Corresponding authors.
E-mail addresses: dmiller@lphys2.chem.utoronto.ca (R.J.D. Miller), guenther.kassier@desy.de (G.H. Kassier).
[1] Present address: Center for Free-Electron Laser Science CFEL, Deutsches Elektronen-Synchrotron DESY, Notkestr. 85, 22607 Hamburg, Germany.

https://doi.org/10.1016/j.ultramic.2022.113579
Received 10 March 2022; Received in revised form 17 June 2022; Accepted 21 June 2022
Available online 22 June 2022

spectrum exhibits a strong peak in the 2-5 eV range, although conventionally all emitted electrons below 50 eV are regarded as SEs [22]. While SE emission is commonly used as a surface sensitive signal in scanning electron microscopy (SEM), it is relatively rarely employed in TEM/STEM [22,23]. Specimen charging, a direct result of SE emission, is however a widely discussed phenomenon in TEM (also LPEM), and has been described and explained in some detail [24–26]. Due to their low energy, the mean free path (MFP) of SEs in a material is in the few nm range, with insulators (e.g. Si_3N_4) generally showing a larger MFP in the order of 10 nm as compared to conductors (e.g. carbon) with less than 5 nm [27]. The ratio of the number of SE leaving a surface to the number of incident primary electrons, or SE emission coefficients σ, are in the range of a few percent, and cause significant SE effects at interfaces, in particular the window:vacuum or window:liquid boundaries [28]. These effects show a strong dependence on the relevant material properties and local potentials. Gupta et al. numerically investigated the effect of differences in SE emission properties on local chemistry at interfaces inside a LC in some detail, confirming that the concentration of important radical species such as e^-_{aq} can be greatly affected in the proximity of solid/liquid interfaces [11]. Experimental studies of such phenomena, including considerations of the role of SE currents emitted into vacuum, are however lacking in the LPEM community.

Herein, we present a systematic comparative study of in situ electron beam induced radiolysis by observing gold nanoparticle (AuNP) growth dynamics for a selection of widely used LC window materials: Si_3N_4, amorphous carbon, and Formvar. AuNP growth dynamics was chosen as the model system as it has been extensively investigated [15,21,29–32]. Si_3N_4 is the most commonly utilized window material in LC research, and therefore an essential component of our study. Carbon, a commonly used substrate in conventional TEM, has been selected here as a cost effective and easier to handle proxy for the more widely employed graphene LC approaches and due to a growing interest in this window material [33,34]. Si_3N_4 and carbon represent two major classes of materials; insulator and conductor, which are expected to exhibit different SE dynamics behavior through the alternate current flow and charge accumulation properties. While Formvar (polyvinyl formal) is commonly used as a sample substrate in conventional TEM, it was recently successfully employed in an liquid-cell/micro-chamber TEM experiment [35]. Therefore to additionally investigate the feasibility of formvar as a LC window, we included it in this study.

We chose anodic aluminum oxide (AAO) support structures similar to what was presented by Lim et al. as a universal LC platform for our investigations [36] . This structure promotes even liquid distribution of a desired thickness over large fields of view by acting as a spacer support. In addition, it creates individually-isolated liquid cells which is ideal in mitigating the migration of radiolytic species, thus providing well defined chemical nanochambers [15,37-39].

2. Results and discussion

2.1. Influence of window material on AuNP growth

The formation of AuNPs requires a transfer of charge from the bulk radiolytic species to the $HAuCl_4$ precursor solution. The reduction of Au^{3+} predominantly occurs with e^-_{aq} due to its large reduction potential (-2.9 V) compared to other reducing species such as hydrogen ($H^\bullet$) and hydroxide (OH^-) radicals at +1.8 and -2.3 V, respectively [40]. Detailed calculations by Schneider et al. suggest a dose rate dependence on the steady state concentration of these species [15]. Our aim is to employ the AuNP growth as a reporter event for the influence of the window material and SE emission on radiolytic species at a constant dose rate.

To observe the nucleation and growth of AuNPs, movies were recorded on a TEM operated at 200 keV, at a fixed dose rate of 24 $e^-/Å^2s$ with an exposure time of 0.5 s per frame and a magnification corresponding to a camera pixel size of 0.34 nm. This was repeated and averaged for three regions in each assembled liquid cell. Each region contains roughly 20 AAO wells that are fully in the field of view. These were selected for further analysis, while the partially cut off wells on the edges were neglected. The growth of AuNPs in each of the selected wells was analyzed and averaged across the three regions. Following the image acquisition, further images were recorded to estimate the apparent scattering liquid layer thickness following a procedure adapted from Azim et al. in which the mean image intensity at two objective apertures was recorded [7]. Representative TEM micrographs showcasing the AuNP growth are depicted in Fig. 1a.

From the micrographs in Fig. 1a, it is clear that the AuNP growth depends on the window material. In particular, Si_3N_4 exhibited particles of uniform size, whereas a broader size distribution was observed for the carbon and formvar windows. To compare the growth with the three window materials, the total hemispherical AuNP volume present in the viewing region was calculated [41]. The results are shown in Fig. 1b. It is apparent that the growth rate of total hemispherical volume with increasing dose is larger for Si_3N_4 as compared with carbon and formvar, which exhibit similar growth.

We observed instances of preferred growth at the AAO pore peripheries, possibly due to preferential in-scattering of SEs at the Al_2O_3: liquid boundary [11]. The consistently observed high growth rate is followed by a plateau likely due to dynamic equilibrium. Considering this, and that minimal growth was observed between the individual wells, we regard the AAO to act as individually sealed liquid-cells.

Two parameters in the bulk liquid that could influence AuNP growth are the concentration of precursor solution and liquid thickness [42,43]. In this case, the 20 mM $HAuCl_4$ solution was the same for all window assemblies. Park et al., Wang et al. observed morphological differences when the liquid layer was thin (< 250 nm) or thick (> 1 μm) [21,44]. In Fig. 1a, no morphological differences such as rods and spurs were observed. Furthermore, for the three liquid cell assemblies, the average liquid thickness of the AAO wells was 97 ± 18, 157 ± 4 nm and 81 ± 8 nm for Si_3N_4, carbon and formvar, respectively. We note that the variation of growth rates between individual wells is significantly lower for formvar. We hypothesize that this is related to higher homogeneity and the material properties.

2.2. Electrical bias dependent growth

We have established a clear influence of the window material on the total hemispherical volume of Au. Scholtz et al. reported how different escape depths of conductive and insulating materials directly influence the SE emission [45]. To investigate the influence that the SE emission, locally composed of SE escape flux (SEEF) and return flux (SERF), has on the radiolytic reduction of Au^{3+}, we applied a bias of -20 V, 0 V, and +20 V to the specimen relative to the holder held at ground potential. A schematic of the setup is shown in Fig. 2a. The AuNP growth for no bias, negative bias, and positive bias are shown in Fig. 2b.

When no bias (0 V) is applied to the window materials (Figs. 1b and 2b, green line), the total hemispherical volume is the greatest for the insulating Si_3N_4 windows, whereas the formvar and carbon grids exhibit a similar growth with increasing cumulative dose.

When we applied a bias of -20 V to the windows, there was a decrease in the growth for carbon, Si_3N_4 and formvar (Fig. 2b, blue line). Remarkably at -20 V, the variation between runs for all windows decreased drastically. SERF therefore not only increases AuNP growth, but also significantly affects the spatial and temporal variation. A bias of +20 V resulted in a major increase in growth for the carbon windows (Fig. 2b, orange line). For the Si_3N_4 and formvar windows, the +20 V bias did not significantly influence the total hemispherical volume. Furthermore, the positive bias resulted in increased inconsistent growth between runs.

As before the two aperture method was used to measure the liquid thickness in lieu of EELS. The liquid thickness and standard error of the mean of three regions are shown in Table 1.

For the respective window materials, we found a comparable

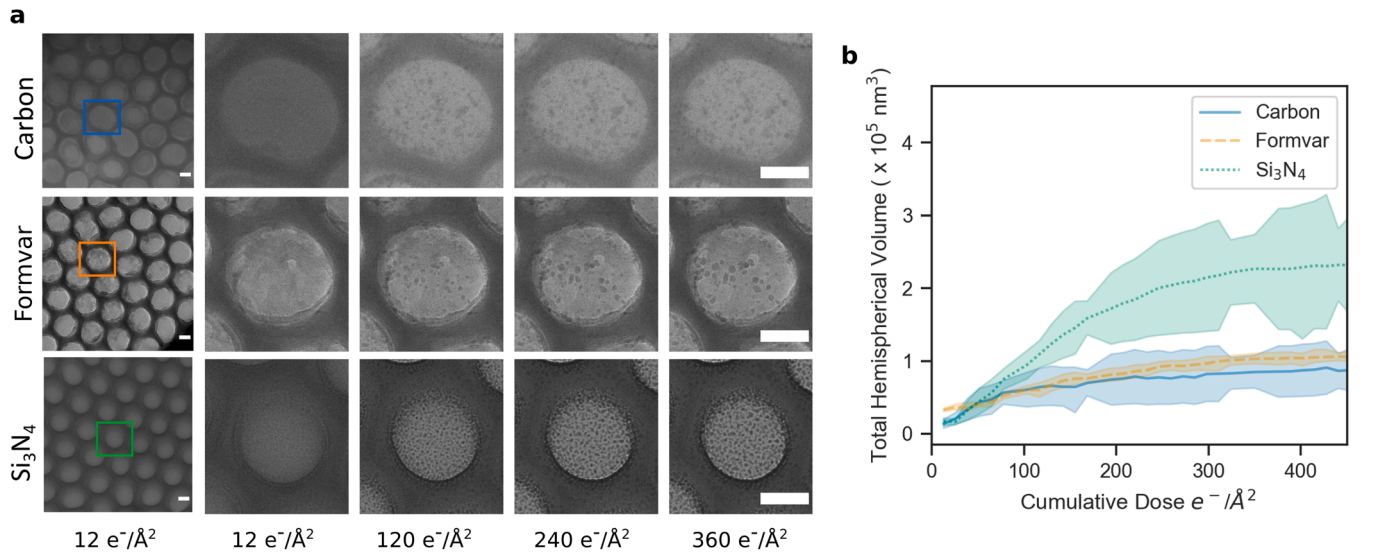

Fig. 1. AuNP growth in assembled AAO liquid cells with carbon, formvar, and Si_3N_4 windows, in which no bias is applied. a) An overview of the imaging area at a cumulative dose of 12 $e^-/Å^2$ is shown in the left column, scale bar 50 nm. The AuNP growth in one AAO well, is highlighted with the colored box. The scale bar of the individual AAO well is 50 nm. b) Average total hemispherical volume of three regions with increased cumulative dose. Shaded regions represent the standard error of the mean.

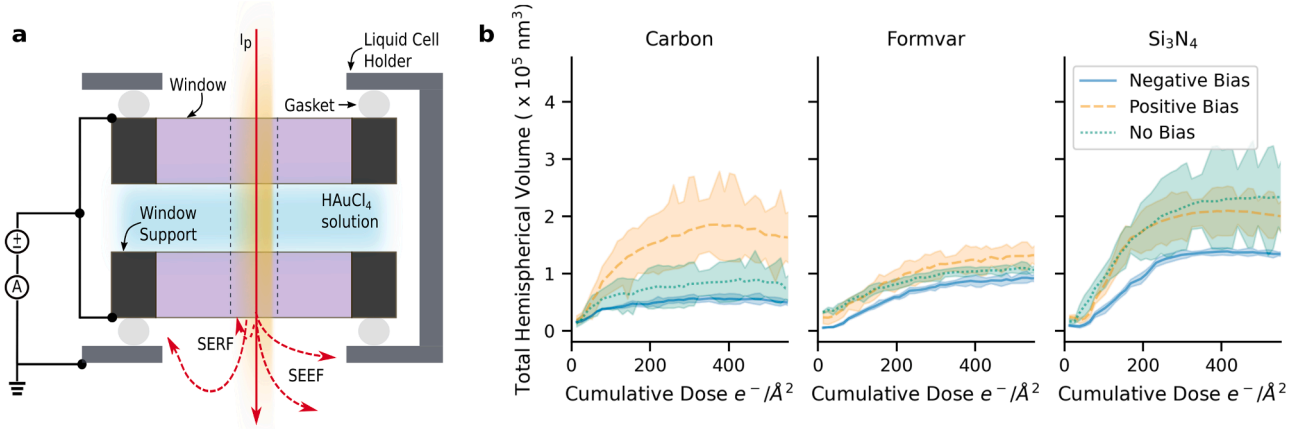

Fig. 2. a) Schematic of the liquid cell holder with the ability to bias the window. b) Influence of bias on AuNPs total hemispherical volume for the three window materials: carbon, formvar, and Si_3N_4 when no bias, 20 V and -20 V was applied. Shaded regions represent the standard error of the mean between three runs.

Table 1
Average liquid thickness (nm) and standard error of mean.

Window	-20 V	20 V	0 V
Carbon	154 ± 1	163 ± 12	157 ± 4
Formvar	92 ± 1	89 ± 5	81 ± 8
Si_3N_4	122±6	108±12	97±18

Table 2
Secondary electron current (σ_{SE}).

Bias (V)	Carbon σSE	Formvar σSE	Si_3N_4 σSE
-20	26.0	0.7	1.5
20	1.7	0.8	1.6
0	25.2	0.4	1.6

average liquid thickness for the no biased and biased runs. This eliminates the possibility that differences in thickness could account for different growth. The fact that the carbon LC assembly with the thickest liquid layer did not produce the greatest volume, suggests that it's the window properties rather than the liquid thickness that is instrumental to the AuNP growth.

2.2.1. SE Escape Current Measurement

To investigate if SEEF and/or SERF is attributable to the different growth profiles observed in Figure 2, the current was measured following the biased movie acquisition. The results of σ_{SE} are shown in Table 2.

Higher σ_{SE} values corresponds to more SEEF escaping towards the vacuum or captured by the holder. The most prominent difference in AuNP growth with the application of a bias in Fig. 2 was in case of a carbon window, which is also reflected in the σ_{SE} values.

With the application of a positive bias (20 V), the σ_{SE} value decreases by an order of magnitude, whereas a negative bias marginally increases σ_{SE}.

Surprisingly, the σ_{SE} values for formvar and Si_3N_4 did not substantially vary with bias, even though locally there is expected to be a significant bias dependency (σ_{SE}) as suggested by our model introduced in the subsequent section. We attribute the results in Table 2 to the

insulating nature of the formvar and Si_3N_4 windows, which hampers current flow to the sourcemeter. Additionally, the formvar window was supported on a 3 mm copper TEM grid and silver paint was applied to the backside of the Si_3N_4. Therefore it is likely that only a small fraction of the SEEF was measured with this setup, making the results in Table 2 misleading in terms of actual microscopic secondary emission dynamics.

2.2.2. Description of the model

In order to understand the bias dependence of SE emission (Table 2) and Au growth from Fig. 2b, we developed a model (Fig. 3) that describes the SE dynamics based on the window properties and external bias. Herein we refer to the carbon LC window as "conductive" and the Si_3N_4 and formvar LC windows as "insulating." In the case of the two insulating window materials, Si_3N_4 has a larger dielectric breakdown strength than formvar and thus supports a higher charge density. This results in larger electric fields and an increase in SERF. Due to the current window thicknesses being larger than the SE escape depths, the influence of window thicknesses is not considered [27].

Since primary beam current (I_p) exposure results in positive window charging due to SE emission, the illuminated region is always positively charged [10,24–26,46]. The global specimen pre-exposure from beam alignments likewise causes the surrounding annular region to initially exhibit a positive charge. The reason why charging also occurs for nominally conductive materials such as carbon is due to the buildup of an insulating contamination layer on the surface [47]. In the case of carbon, this causes a slightly positive and negative charging inside and outside the illuminated region, respectively [48–50]. The insulating Si_3N_4 is therefore qualitatively similar to carbon in terms of charging effects, the difference lies mainly in the magnitude. The combined charge states of the center and annular region result in an electric field (Fig. 3, potential lines), which in turn affects the SEEF and SERF.

In the case of a negative bias, both conductive and insulating windows exhibit very little SERF in the annular region. Thus, the initial positive charge is preserved, damping the retention electric field due to the highly charged center (Fig. 3, potential lines). This results in increased SEEF and a decrease in solvated electrons. Due to more charging in the insulating window, the SEEF is larger with the conductive window, as shown in Table 2. This model not only explains the reduced growth but also the low variation between runs with negative bias in Fig. 2 as the effect of SERF electrons, which are highly sensitive to locally changing surface properties are suppressed.

In case of no bias, some SERF is attracted to the positively charged annular region, resulting in partial or full neutralization. As a result, the retention electric field in the center region is no longer damped, resulting in reduced SEEF. The reduction in SEEF with the removal of the negative bias, results in an increase in SERF for both the conductive and insulating windows (Fig. 3) and an increase in AuNP growth (Fig. 2). Additionally, in the case of the conductive window, some SERF from the annular region is conducted back to the center through radial currents (I_c) in the window material [25,51] (Fig. 2 Carbon). A positive bias in turn leads to even larger SERF in the annular region and negative charging; this in turn leads to an enhancement of the center electric field, further reduction of SEEF as measured by σ_{SE}(Table 2), and concomitant enhanced AuNP growth. The enhanced radial return current (I_c) in the conductive window in addition to the more efficient distribution of external bias potential could explain the relatively large growth enhancement seen for the positively biased carbon LC in Fig. 2.

Considering this, a more conductive graphene window would be influenced even more by the positive and negative biases than the carbon window. With the insulating windows, we attribute the minor changes in AuNP growth between no bias and positive bias (Fig. 2, formvar and Si_3N_4) to be due to the lack of radical return currents (I_c).

Loh et al. and Tan et al. reported an increase in $AuCl_4^-$ concentration at positively charged Si_3N_4 surfaces [30,52]. This concentration gradient of precursor ions leads to increased growth at the window-liquid interface [30,42,43,52]. Mehdi et al. attributed this to an increase in the electric field at the window: liquid interface [53]. Therefore we propose for the conductive and insulating window materials presented here, the difference in growth observed in Fig. 2 is due to the different charging properties, SEEF, and SERF.

2.2.4. Simulating the surface electric field and SERF

In order to quantify the predictions of our model, we performed electric field calculations and particle tracking simulations. Briefly, the SE emission (SEE) region was modelled as a circular patch with a 1 μm radius held at constant positive potential, surrounded by a large annular

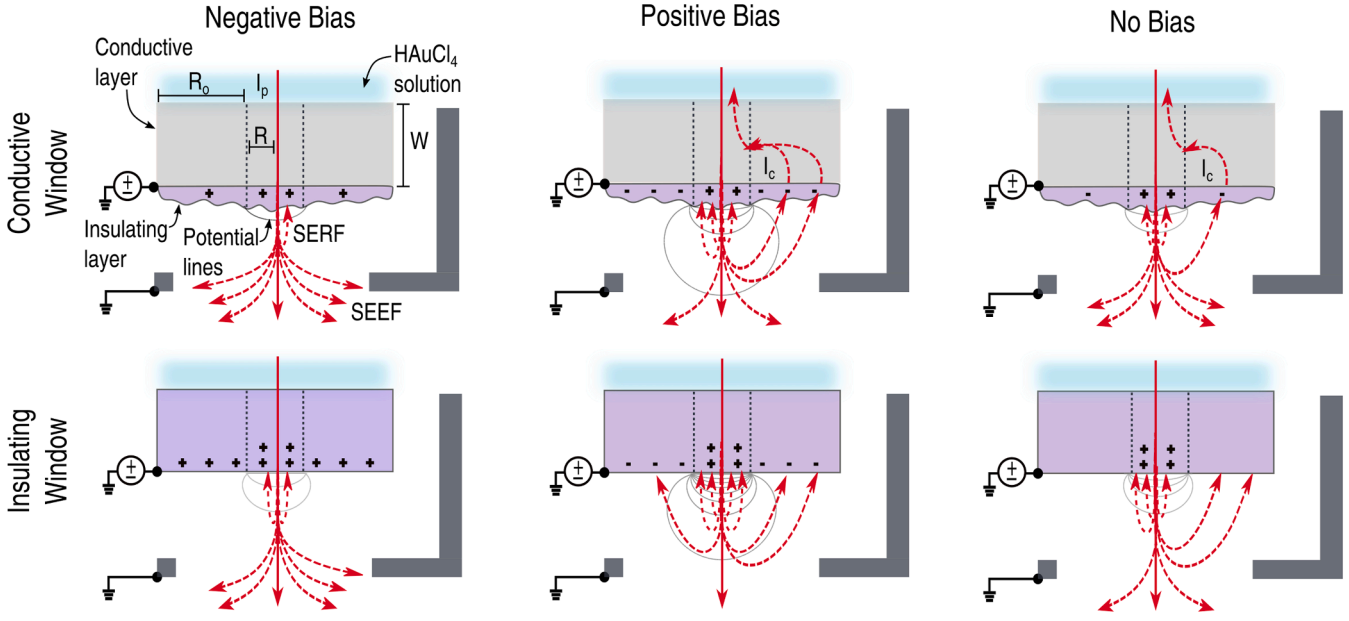

Fig. 3. Schematic of the SE return flux (SERF), escape flux (SEEF) and electric field potential lines in the conductive (gray) and insulating (purple) window materials in the case when a negative bias (left column), positive bias (middle column) and no bias (right column) is applied to the LC assembly and the outside holder is set to ground and based off of the simulation parameters: beam radius (R) of 1 μm, annulus (R_o) of 50 μm, window height (W) of 10 nm. Also shown are the radial conduction (I_c) from the returning electrons.

region with varying charge depending on the different cases 1 a-c and 2 a-c in Fig. 4.

Fig 4, 1 a-c and 2 a-c depict the simulated SERF for negative (a), positive (b) and zero (c) bias. The potential magnitude in both the center (irradiated) region and surrounding annulus was set larger in case of the insulating window compared with the conductive one. Setting the annulus potential negative, zero and positive, corresponding to positive, zero and negative annulus bias respectively yields the SERF scatter plots in Fig. 4 a-c. Clearly, SERF is significantly higher in all regions for the insulating window compared to the conductive window. Also, an increasing positive bias leads to increasing SERF in both the center and annulus regions. The radially averaged histograms (Fig. 4d) depict the fraction of SERF from the total initial secondary electron emission current density (SEE) at the plane of emission (SERF/SEE). A significant proportion between 0.1 - 0.25 occurs in the center region for all cases, with an increase in SERF with increasing positive bias in both the center and annular region up to 3 μm. The simulated potential maps are represented in the SERF/SEEF schematic (Fig. 3) and in the SI. The depth of the electron retaining potential increases with increasing positive bias, and is also deeper for the insulating window compared with the conductive one, with corresponding effect on the SERF. Our simulations are thus in line with the window material and bias dependent AuNP growth results, assuming 1) that SERF increases the concentration of solvated electrons in the liquid layer and 2) that the radial currents (I_c) increase with conductivity (Fig. 3).

2.2.5. SE Return Flux (SERF) outside of the beam

Our model relies on the balance between SEEF and SERF, with both occurring inside the beam and only SERF outside the region of illumination. The previous σ_{SE} measurements show that both the SEEF (Table 2) and AuNP growth (Fig. 2 B) vary between window material and applied bias. However, due to the design of the liquid cell holder, direct measurement of SERF inside and outside of the beam was not possible.

To qualitatively investigate SERF outside of the beam, images with a lower magnification (larger field of view) at 1.25 nm pixel size (10.000 nominal magnification) were acquired before and after recording the AuNP growth for two minutes at high magnification (pixel size of 0.34 nm, 40.000 nominal magnification) at a dose rate of 24 $e^-/Å^2s$. [2]. After the movie acquisition, a high magnification image was acquired of AAO wells both inside and outside of the originally illuminated area. Representative micrographs for carbon and Si_3N_4 are shown in Fig. 5.

The columns a depict the periphery of the beam (red line) and a region selected to showcase AAO wells inside and outside of the beam (white box). A high magnification image of this region is shown in column B. To highlight the growth outside of the beam, representative AAO wells are shown in last columns C and D. With both window materials and all biases, growth is observed outside of the irradiated region (red circle). Furthermore, in the case of Si_3N_4 the polydispersity of the particle size increases outside of the irradiated area (SI Fig. 2).

The resolution of the lower magnification (1.25 nm pixel size) before and after images did not allow for individual particle picking as previously carried out. Therefore to determine if particle growth occurred further beyond the beam, a Structural Similarity Index Measurement (SSIM) was calculated based off of the luminance, contrast and structure of the before and after images [54]. This was repeated for three regions. The averaged values ranging from 0 to 1 were calculated, with 1 corresponding to no change between the two images [55]. The SSIM results are shown in Table 3.

Following two minutes of irradiation at 24 e-/Å 2s a bias of 20 V resulted in the most change in the periphery followed by 0 V and -20 V for the Si_3N_4 and carbon windows. Growth outside the region of illumination has been observed for Ag nanoparticles and metal-organic frameworks (MOFs) between two Si_3N_4 windows [56, 57]. In these cases, the growth was attributed to the diffusion of radical species. As the simulations (Fig. 4) show SERF/SEE beyond the beam and we consider the AAO to act as individually sealed micro-wells, we propose SERF to play a larger role than diffusion. Therefore these results serve as a qualitative basis that the proposed model that AuNP growth increases with SERF and bias is plausible.

2.3. Gated AuNP Growth

Sample bias dependence of AuNP growth was verified in the previous section, and a model was presented which predicts bias dependent variation of SEEF and SERF that agrees qualitatively with observed emission currents and AuNP growth. There was however no direct measurement of the proposed electrostatic fields resulting from charge buildup. To provide additional proof for the correlated modulation of AuNP growth and SEEF/SERF, we implemented a setup allowing for a more direct study as illustrated in Fig. 6. Instead of the bias modulation of long range SE emission escaping in the vacuum, this structure allows

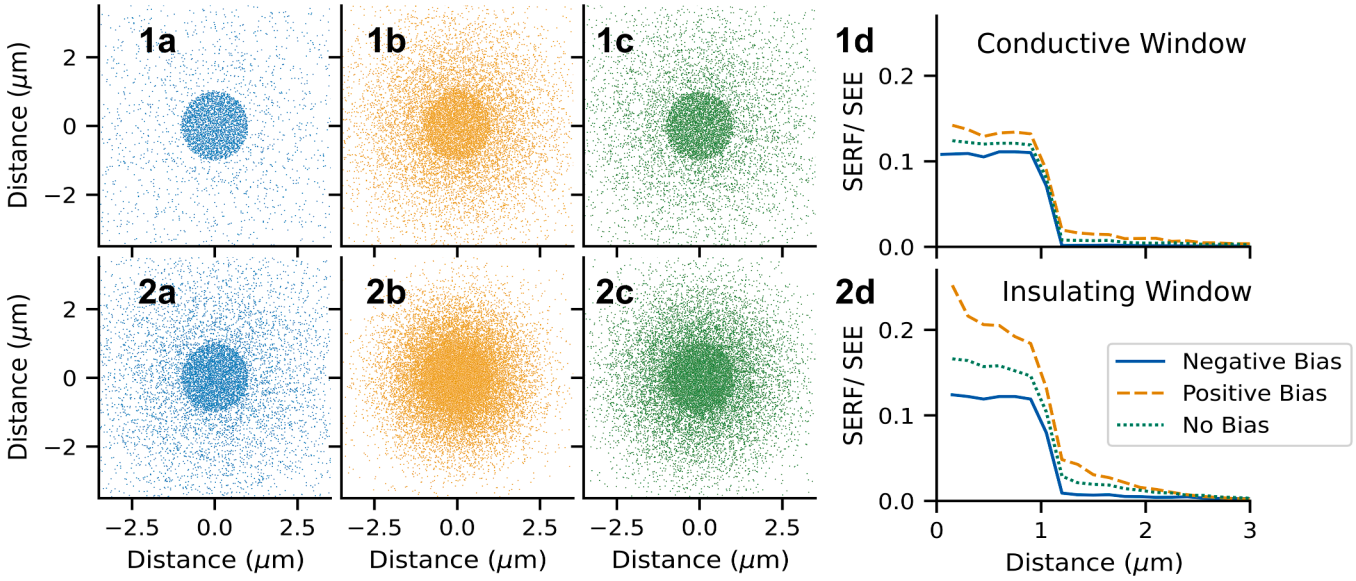

Fig. 4. Simulated SERF for conductive (1) and insulating windows (2). a-c depict the simulated SERF for negative, positive and zero bias, respectively. 1d and 2d are the corresponding radial histograms from the center to 3 μm for conductive and insulating windows, showcasing the ratio of SERF to SEE particle density.

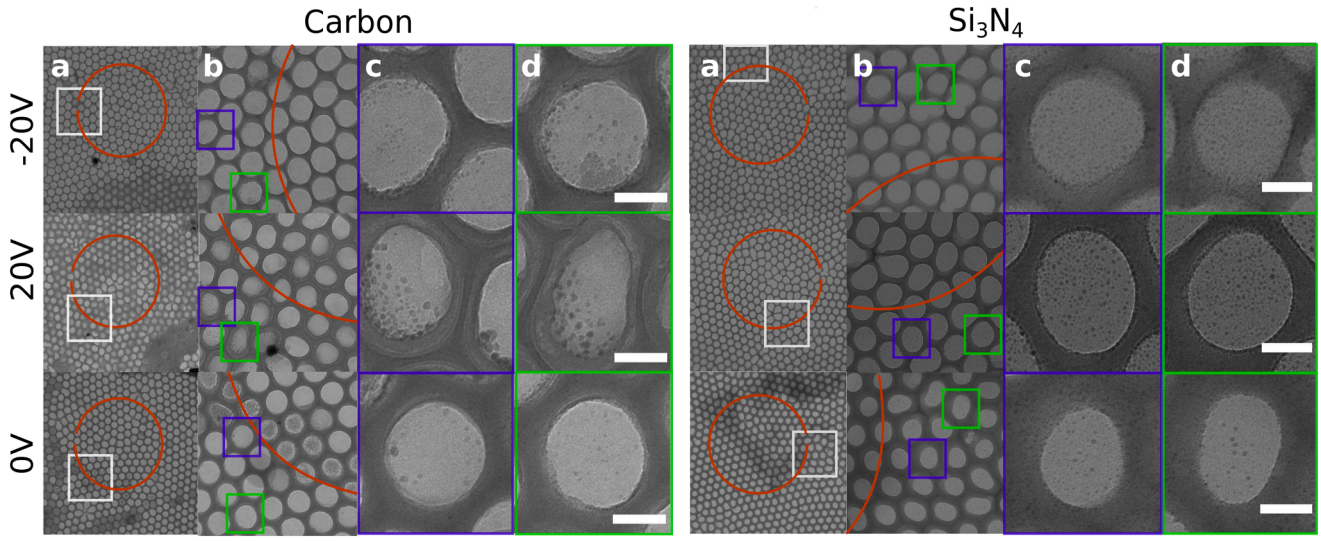

Fig. 5. a) AuNP growth after two minutes of irradiation in carbon and Si_3N_4 liquid cells. The red circle represents the periphery of the beam. The white box represents the region inside and outside of the beam. Micrographs of the respective regions are shown in column b while representative AAO wells are displayed in columns c and d. The scale bar represents 50 nm in all instances.

Table 3
SSIM values for carbon and Si_3N_4 outside of beam.

Voltage(V)	Si_3N_4	Carbon 20
20 V	0.336 ± 0.021	0.275 ± 0.020
0	0.368 ± 0.007	0.288 ± 0.018
-20	0.373±0.005	0.290±0.010

for active control of large electric fields within the Si_3N_4 window itself through a 5 nm carbon layer deposited on the vacuum facing side of the window [24]. A standard 3 mm carbon TEM grid was used to seal the assembly at the top side. The entire assembly was biased at 10 V relative to ground in order to minimize the SEEF on both the carbon and the C-Si_3N_4 side. Electric field modulations in the Si_3N_4 layer were achieved by applying a bias of 10 ± 1 V (9 V, 10 V and 11 V) to the carbon coating resulting in the biases of $V_A = V_B$, $V_A < V_B$, and $V_A > V_B$ respectively. As before, we measured the AuNP growth, liquid thickness and calculated the total hemispherical volume. Fig. 7 depicts the results.

The average liquid thickness within the AAO wells was 166 ± 13, 166 ± 11, and 180 ± 6 for $V_A = V_B$, $V_A < V_B$, and $V_A > V_B$ respectively. This again ensures the observed trends are not due to liquid layer fluctuations. Relative to $V_A = V_B$, setting $V_A < V_B$ and $V_A > V_B$ resulted in an increase and decrease in growth, respectively. This implies modulation of the SEEF and SERF at the liquid:Si_3N_4 boundary. Consider first the equal bias case (Fig. 6); SE emission in the Si_3N_4 layer leads to electron depletion and positive charging until an equilibrium between SE flux from liquid to Si_3N_4 and vice versa is reached. Applying a relative negative bias at the carbon gate electrode results in an additional electric field in the Si_3N_4 which directs a portion of SEs generated in the Si_3N_4 layer into the liquid layer. Similarly, some SEs injected from the liquid layer into the Si_3N_4 are directed back into the liquid layer, leading to increased reduction of Au^{3+} ions. For the positive bias case, SEs generated in the Si_3N_4 are less likely to be injected into the liquid layer due to the applied electric field attracting electrons to the carbon gate electrode. Also, SEs injected from the liquid layer into the Si_3N_4 are less likely to return. The Au growth curves in Fig. 7 clearly show the expected differences subject to the applied biases.

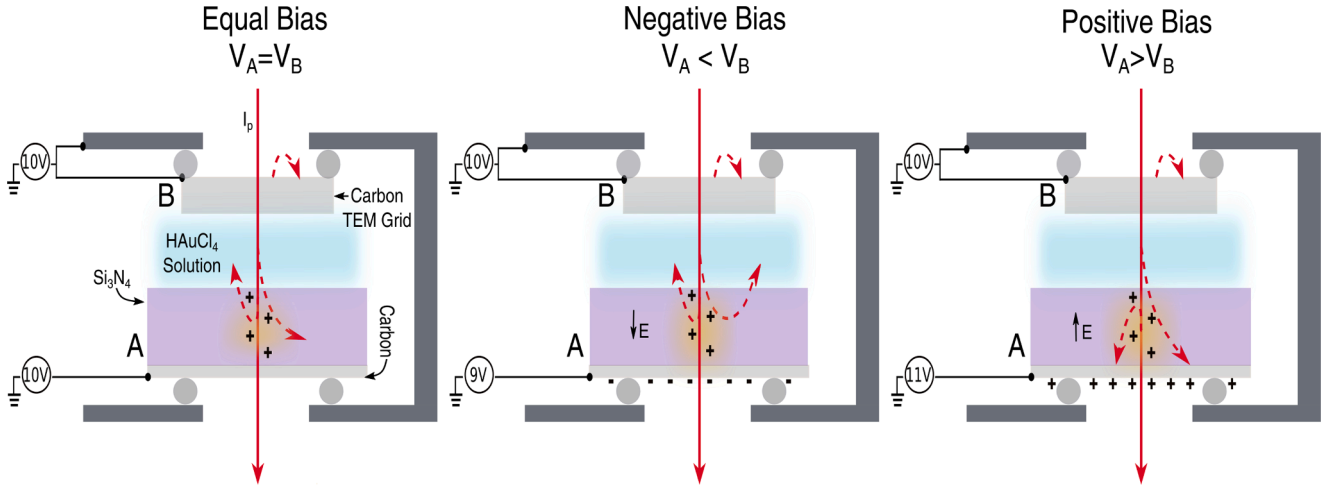

Fig. 6. AuNP growth from biased gating. Electrical hookup for modulating AuNP growth for the different biases and schematic of suggested SE electron paths in response to different applied gating voltages.

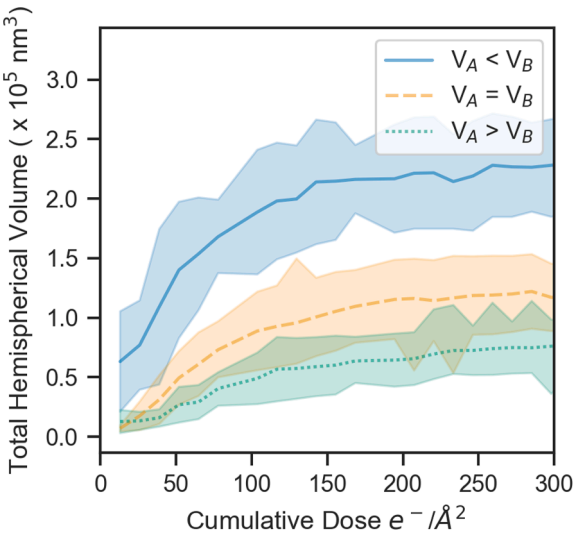

Fig. 7. Total hemispherical volume with increased cumulative dose for AuNP grown by modulating the bias applied to the C-Si_3N_4 window. The carbon TEM grid and holder was kept at 10 V, whereas the C-Si_3N_4 window was either equally biased, negatively or positively biased towards carbon or $V_A = V_B$, $V_A < V_B$, and $V_A > V_B$ respectively.

3. Conclusion

Herein the commercially available AAO sheet allowed for the removal of difficult nano-fabrication steps required for nano-well fabrication. We showed that the AAO adheres to carbon, formvar, and Si_3N_4 windows, and that formvar is a suitable window material for 3 mm liquid cells. Direct comparison of the beam induced radiolysis with the three LC assemblies revealed that the window conductivity influences the total AuNP hemispherical volume, with increasing conductivity decreasing AuNP growth. Therefore these results affirm the use of conductive window materials as a way to mitigate adverse beam effects. Through biasing the window we demonstrated the ability to increase or decrease AuNP growth. Although the conductive carbon window was most influenced by biases, generally a bias of 20 V increased the growth and not only -20 V decreased the total hemispherical AuNP volume but also decreased the variation between runs. The ability to bias the LC holder will allow for improved control of future LC experiments. Our custom made liquid cell holder also allowed for the measurement of σ_{SE}. Although the σ_{SE} was low for the insulating windows, carbon showed a decrease by an order of magnitude with the application of a positive bias. We attributed the variations in total hemispherical volume with different window materials and biases to the balance between SERF and SEEF. This was confirmed through our model and simulations that depict an increase in SERF within and outside the beam region. The micrographs outside the beam annulus and SSIM qualitatively validated that the increase in SERF can result in increased growth due to more reducing species in the bulk.

Through the carbon:Si_3N_4-carbon coated LC assembly we controlled electric fields within the Si_3N_4 window and modulation of AuNP growth. Furthermore, we determined that applying a bias is a viable way to modulate beam induced AuNP growth, implying that LCs in general can be treated as an electrochemical cell. We note that surface effects and the different nucleation barriers in the three window materials complicate AuNP growth. However, we have focused on the growth of AuNPs that provides information on the excess solvated, reducing, electron conditions in the near surface region. Overall, these results can serve as a template for future LPEM experiments and exemplify that when investigating or mitigating sample damage or beam induced radiolysis in the bulk, the window material must be taken into consideration.

4. Experimental

4.1. Transmission electron microscopy

TEM was performed on a JEOL JEM-2100 operated at 200 keV. Bright-field micrographs were recorded at room temperature with a TVIPS TemCam F216 camera with no energy filter.

4.2. Formvar TEM grid preparation

The formvar TEM grid preparation was based off of the procedure described by Both et al. [58]. Herein a drop of 0.3% solution of formvar dissolved in 1,2-dichloroethane was dropcast onto water in a glass dish (diameter 9 cm) using a glass pipette. The formvar solution spread on top of the water surface. Glow discharged, 400 mesh TEM copper grids (purchased from Plano GmbH) were placed on top of the floating formvar film. To remove the TEM grids, the back-side of the floating TEM grids were touched with a piece of parafilm cut to the dimensions of the floating grids. This allowed for the easy removal of all of the formvar coated grids. The grids were left to dry for 30 min before subsequent use.

4.4. AAO Fabrication

The AAO liquid cell fabrication was based off of Lim et al. [36]. A square sheet of AAO from the as-provided 15 × 15 mm membrane, cut with a razor blade on a glass slide with the AAO side up and poly(methyl methacrylate) (PMMA) side facing down. The sheet has inter-pore distances of 125 nm, pore diameters between 70-90 nm and a thickness of 130 nm (UT125-079-130, from top membranes technology). A 0.3 μl drop of ddH_2O was placed on the center of the 3 mm TEM grid (formvar or carbon coated S160 mesh 400 TEM grids from PLANO). The grid was touched to the AAO sheet, leaving the PMMA on top. The liquid was allowed to evaporate and the grid was flipped upside down and placed in a custom TEM grid holder that accommodates 12 grids (Fig. 8c). This holder was placed in a glass petri-dish, acetone (Sigma Aldrich) was added to dissolve the PMMA. The acetone was replaced two times over the course of four hours.

In the case of the Si_3N_4 window, a similar procedure was applied except the Si_3N_4 chips were glow discharged for 30 seconds. To account for the increased hydrophilicity and liquid spreading, 0.5 μl drop of ddH_2O was placed on the center of the nitride chip. Furthermore the chip was placed in a custom liquid cell chip holder, face side up (Fig. 8a). The top clamp acted to secure the AAO to the Si_3N_4 chip (Fig. 8b).

4.5. Carbon coating on Si_3N_4 chips

The Si_3N_4 chips were glow discharged for 30 seconds and subsequently placed in a Leica ACE60 carbon coater. A 5 nm layer of carbon was deposited to the back side of the AAO containing Si_3N_4 chips.

4.6. Liquid cell holder for AuNP growth

The liquid cell holder described in Azim et al. [7] was modified to improve with a new gaskets and an adapter to accommodate using 3 mm TEM grids. These modifications are depicted in Fig. 9.

Additionally this holder was modified with an electrical feedthrough

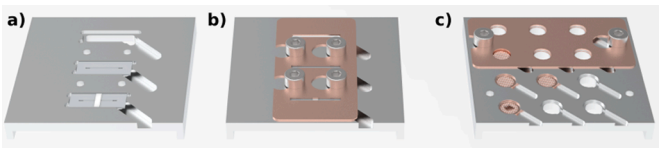

Fig. 8. Holder used for fabricating Si_3N_4, formvar and carbon AAO windows. a) holder with Si_3N_4 chip containing AAO face side up, b) holder with lid, c) holder for standard 3 mm TEM grids with AAO face side down.

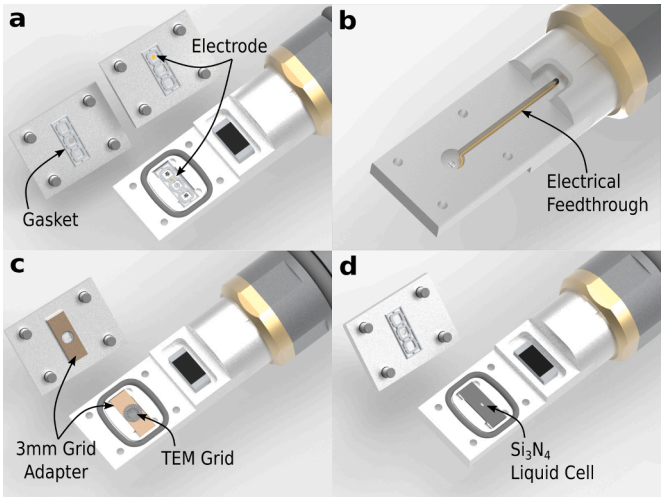

Fig. 9. Modifications to liquid cell holder. a) gaskets on the lid and bottom with the electrode on the right lid and holder. b) backside of holder showing electrical feedthrough. c) adapter for 3 mm TEM grids. d) Si_3N_4 liquid cell.

(Fig. 9b) to include two electrodes, one in contact with the bottom liquid cell chip and the second connected to the outside holder through the lid (Fig. 9a).

4.7. Liquid cell assembly

All assemblies took place outside of the liquid cell holder and used 0.3 μl drop of 20 mM $HAuCl_4$ (chloroauric acid, $HAuCl_4$ (Sigma Aldrich) dissolved in deionized (DI) water). In the case of formvar and carbon, the $HAuCl_4$ solution was applied to an AAO containing TEM grid held by tweezers, a second TEM grid with a cut flat side, was placed on top of the $HAuCl_4$ grid. The grids came together. The assembled grid was sandwiched between the two copper adapters in the liquid cell holder (Fig. 9c). For the formvar and carbon TEM grids, the copper adapter conveniently ensured that the two windows are in contact with one another. However, in order for the Si_3N_4 liquid cell chips to be connected to the electrode, a small amount of silver paint was placed on the backside of the bottom chip. Silver paint was applied to the periphery of the assembled liquid cell to guarantee electrical contact between the chips.

4.8. Current calibration

To account for drift in the initial calibration of the current density readout on the phosphor viewing screen of the JEOL JEM-2100 TEM, a correction factor similar to what was outlined in Azim et al. was determined [7]. The liquid cell holder was used as a Faraday cup by loading it with a 0.3 mm thick laser cut copper chip with a 0.5 mm hole in the center so that the beam can be made either to pass through un-scattered, or fully absorbed by the copper plate for current measurement. The generated electron beam was initially passed through the center and the resulting phosphor screen current as displayed by the TEM was recorded. Note that the readout is displayed as a current density rather than a current, assuming homogeneous illumination of the entire phosphor screen. Multiplying this readout by the screen area $A_s = \pi r_s^2$, where $r_s = 8$ cm, the corresponding current was calculated. The sample holder was then moved so that the beam is fully absorbed by the copper plate for precise current measurement. Biasing the copper plate at +20 V minimized the loss of secondary electrons which could affect the measurement. The absorbed current was measured with a Keithley 2614B sourcemeter, $I_{true} = I_{beamon} - I_{beamoff}$. The beam current was varied in the range of 1-110 nA, and the correction factor $f = I_{screen}/I_{meas}$ =0.74 ± 0.03 was extracted from a linear fit to the plot of phosphor against Faraday cup currents with an R^2 value of 0.997. From hereon the correction factor was used to calculate the actual primary current.

4.9. Secondary electron current

To calculate the SE coefficient (σ_{SE}), the screen (I_p) and the secondary emission current (I_{emit}) as measured by the sourcemeter currents were recorded when biases of ± 20 and 0 V were applied to the windows or holder. σ_{SE} was calculated by

$$\sigma_{SE} = \frac{I_{emit}}{I_P} \tag{1}$$

4.10. AuNP Growth analysis

To correct for drift during image acquisition, the frames were aligned with the ImageJ Linear Stack Alignment with SIFT plugin and subsequently color inverted. A python script based off of "Custom Feature Detection: Bubble tracking in 2D foams" which uses trackpy was used to find and link the particle growth [59]. As we were only considering the particle growth within each AAO well, the first step involved thresholding the stack of micrographs for one movie and cropping the individual wells that were not touching the periphery of the imaging area. Picking of the AuNP involved an initial thresholding of the individual AAO well. The AuNPs were marked in each frame depending on whether the region area was greater or equal to 16 pixels. Trackpy was used to connect the particles between each frame. To remove noise marked as a particle, the tracked particles were discarded if they disappeared for two frames and were present in less than 20 frames. This procedure was repeated for the individual wells from one movie. As the aim was to assess the overall AuNP growth in the movie, we did not discard windows with minimal to no AuNP growth. The total hemispherical volume of AuNPs was calculated by:

$$V = \sum \frac{2}{3}\pi R^3 \tag{2}$$

with R as the radius of the AuNP.

4.11. Liquid thickness

Following the acquisition of the AuNP growth in a region, we used a variation of the intensity ratio method as described in Azim et al. to record the liquid thickness [7]. This method is used in lieu of having EELS. In case of the assembled AAO liquid cell, the original intensity ratio method applicable for large area homogeneous samples does not apply since large angle scattered electrons would add a significant background, altering the signal. To mitigate this effect, we used a two aperture approach wherein the intensity ratio of two images was recorded

$$r_{total} = \left(\frac{Int_1}{Int_2}\right)_{total} \tag{3}$$

the two different objective apertures are compared, allow for an intensity ratio map with sub-frame resolution to be constructed. The total thickness formula for this case becomes

$$t = \frac{\log(r_{total})}{(1/l_2) - (1/l_1)} \tag{4}$$

where l_2 and l_1 are the mean free path of electron scattering to angles beyond 8.75 mrad (522 nm) and 12.6 mrad (718 nm) in water respectively, Int_2 and Int_1 are the mean intensity for the l_2 and l_1 images.

To subtract the window thickness, r_{win} was introduced:

$$r_{win} = \left(\frac{Int_1}{Int_2}\right)_{window} \tag{5}$$

which takes the average, Int_1/Int_2 intensities for two windows, 1.017 ± 0.003, 1.053 ±0.002, 1.011 ± 0.002 for formvar, Si_3N_4, and carbon respectively. making the final equation for liquid layer calculation:

$$t_{liquid} = \frac{\log(r_{total}) - \log(r_{win})}{(1/l_2) - (1/l_1)} \quad (6)$$

4.12. SERF simulation

The LC window and beam-induced charge layer was simulated as a central circular disc (primary beam area) at a positive potential surrounded by an annulus at a different potential, the value and magnitude depends on the different cases considered in Fig. 3. The disc and annulus were assumed to be conductors. The thickness and distance to the grounded plane, disc and annulus is 10 nm, and outer radii are 1 μm and 50 μm, respectively. These are floating above and not in electrical contact with a conductive ground plate representing the liquid sample. For Si_3N_4 and carbon we assumed a central disc potential of 2 V and 1 V respectively, based on the assumption that the insulating

Si_3N_4 layer has a larger electrical breakthrough voltage than carbon. The corresponding assumed breakdown field strengths are in the order of 10^6 V/cm, which is realistic for thin film insulators, Si_3N_4 in particular [60]. The outer annulus region potential was in the range of -1 V to +1 V, and -0.5 V to +0.5 V for Si_3N_4 and carbon, respectively.

To account for external bias effects, we applied an additional field of 0.04, 0 and -0.04 MV/m for positive, zero and negative bias, respectively. We calculated the electric fields for the 6 different scenarios using the Poisson Superfish set of codes [61]. For more electric field simulation details, refer to the SI. The electric fields were then fed into a particle tracking simulation using the ASTRA code [62] to predict the SEEF and SERF dynamics based on our model. Here, the SE emission distribution was assumed to be spatially uniform over the central disc emission region (radius 1 μm) with a transverse normalized emittance of 1 μrad·mm. A total of 100.000 particles were used for the simulations for good statistics. The energy distribution was assumed to be of the form [22].

$$\frac{dN_{SE}}{dE_{SE}} \propto \frac{1}{E_p} \frac{E_{SE}}{(E_{SE} + \varphi_w)^4} \quad (7)$$

where the left hand side of the equation is the secondary electron distribution, E_p, E_{SE} and φ_w are the primary electron energy, secondary electron energy and work function, respectively. The peak of this distribution is given by $E_{p,SE} = \varphi_w/3$. We assumed an emission peak $E_{p,SE}$ at 3 eV and cutoff at 50 eV. We take this distribution to be a reasonable average of known SE emission energy spectra of various materials, although this equation strictly only applies to metals [22]. For further details including ASTRA input files and Poisson Superfish input files/fieldmaps, refer to the SI.

4.13. Structural similarity index measurement (SSIM) calculation

Before and after recording the AuNP growth movie for 2 min with a beam diameter of 1.4μm and camera pixel size of 0.34 nm, micrographs in focus and at a 4 micron defocus were acquired at a pixel size of 1.25 nm (10 K). These lower magnification micrographs are used to observe changes in the periphery of where the AuNP movie was acquired. A python script was used to calculate the SSIM value (from scikit-image). First the micrographs were aligned to account for beam and stage drift. These images were used as is with skimage.metrics.structural similarity. For only the beam or only the periphery, a representative area image showing the movie region was used as a mask.

Abbreviations

AuNP, TEM, LPEM, LC, e^-_{aq}, SERF, SEEF, SEE, MFP, AAO

Declaration of Competing Interest

The authors declare the following financial interests/personal relationships which may be considered as potential competing interests:

Lindsey A. Bultema reports financial support was provided by Joachim Herz Foundation. Eike C. Schulz reports financial support was provided by Joachim Herz Foundation. Eike C. Schulz reports financial support was provided by German Research Foundation.

Acknowledgement

The authors gratefully acknowledge the support provided by the Max Planck Society and the Joachim Herz Foundation (Biomedical physics of infection) (E.S.; L.B.). Additional funding was supported by the DFG via grant No. 458246365 to E.S.

Supplementary materials

Supplementary material associated with this article can be found, in the online version, at doi:10.1016/j.ultramic.2022.113579.

References

[1] *Liquid Cell Electron Microscopy*; Advances in Microscopy and Microanalysis, Cambridge University Press, 2016.
[2] H.-G. Liao, H. Zheng, Liquid cell transmission electron microscopy, Ann. Rev. Phys. Chem. 67 (2016) 719–747. PMID: 27215823.
[3] S.M. Rehn, M.R. Jones, New strategies for probing energy systems with in situ liquid-phase transmission electron microscopy, ACS Energy Lett. 3 (2018) 1269–1278.
[4] N. de Jonge, N. Poirier-Demers, H. Demers, D.B. Peckys, D. Drouin, Nanometer-resolution electron microscopy through micrometers-thick water layers, Ultramicroscopy 110 (2010) 1114–1119.
[5] N. De Jonge, F.M. Ross, Electron microscopy of specimens in liquid, Nat. Nanotechnol. 6 (2011) 695–704.
[6] G. Zhu, Y. Jiang, W. Huang, H. Zhang, F. Lin, C. Jin, Atomic resolution liquid-cell transmission electron microscopy investigations of the dynamics of nanoparticles in ultrathin liquids, Chem. Commun. 49 (2013) 10944–10946.
[7] S. Azim, L.A. Bultema, M.B. de Kock, E.R. Osorio-Blanco, M. Calderoń, J. Gonschior, J.-P. Leimkohl, F. Tellkamp, R. Bu ̈cker, E.C. Schulz, et al., Environmental liquid cell technique for improved electron microscopic imaging of soft matter in solution, Microsc. Microanal. 27 (2021) 44–53.
[8] S. Keskin, P. Kunnas, N. de Jonge, Liquid-phase electron microscopy with controllable liquid thickness, Nano Lett. 19 (2019) 4608–4613.
[9] N. de Jonge, Theory of the spatial resolution of (scanning) transmission electron microscopy in liquid water or ice layers, Ultramicroscopy 187 (2018) 113–125.
[10] R. Egerton, Radiation damage to organic and inorganic specimens in the TEM, Micron 119 (2019) 72–87.
[11] T. Gupta, N.M. Schneider, J.H. Park, D. Steingart, F.M. Ross, Spatially dependent dose rate in liquid cell transmission electron microscopy, Nanoscale 10 (2018) 7702–7710.
[12] E. Sutter, B. Zhang, S. Sutter, P. Sutter, In situ electron microscopy of the self-assembly of single-stranded DNA-functionalized Au nanoparticles in aqueous solution, Nanoscale 11 (2019) 34–44.
[13] J. Zečević, J. Hermannsdörfer, T. Schuh, K.P. de Jong, N. de Jonge, Anisotropic shape changes of silica nanoparticles induced in liquid with scanning transmission electron microscopy, Small 13 (2017), 1602466.
[14] K. Gnanasekaran, H. Chang, P.J. Smeets, J. Korpanty, F.M. Geiger, N.C. Gianneschi, In situ Ni2+ stain for liposome imaging by liquid-cell transmission electron microscopy, Nano Lett. 20 (2020) 4292–4297.
[15] N.M. Schneider, M.M. Norton, B.J. Mendel, J.M. Grogan, F.M. Ross, H.H. Bau, Electron–water interactions and implications for liquid cell electron microscopy, J. Phys. Chem. C 118 (2014) 22373–22382.
[16] H. Cho, M.R. Jones, S.C. Nguyen, M.R. Hauwiller, A. Zettl, A.P. Alivisatos, The use of graphene and its derivatives for liquid-phase transmission electron microscopy of radiation-sensitive specimens, Nano Lett. 17 (2017) 414–420. PMID: 28026186.
[17] S. Keskin, N. de Jonge, Reduced radiation damage in transmission electron microscopy of proteins in graphene liquid cells, Nano Lett. 18 (2018) 7435–7440.
[18] J.M. Yuk, J. Park, P. Ercius, K. Kim, D.J. Hellebusch, M.F. Crommie, J.Y. Lee, A. Zettl, A.P. Alivisatos, High-resolution EM of colloidal nanocrystal growth using graphene liquid cells, Science 336 (2012) 61–64.
[19] C. Wang, Q. Qiao, T. Shokuhfar, R.F. Klie, High-resolution electron microscopy and spectroscopy of ferritin in biocompatible graphene liquid cells and graphene sandwiches, Adv. Mater. 26 (2014) 3410–3414.
[20] E. Alizadeh, L. Sanche, Precursors of solvated electrons in radiobiological physics and chemistry, Chem. Rev. 112 (2012) 5578–5602. PMID: 22724633.
[21] J.H. Park, N.M. Schneider, J.M. Grogan, M.C. Reuter, H.H. Bau, S. Kodambaka, F. M Ross, Control of electron beam-induced Au nanocrystal growth kinetics through solution chemistry, Nano Lett. 15 (2015) 5314–5320.

[22] L. Reimer, *Scanning Electron Microscopy*; Springer Series in Optical Sciences, Springer, 1998.
[23] D.R.G. Mitchell, G. Casillas, Secondary electron imaging in an aberration-corrected STEM, Microsc. Today 24 (2016) 22–27.
[24] R.M. Glaeser, K.H. Downing, Specimen charging on thin films with one conducting layer: discussion of physical principles, Microsc. Microanal. 10 (2004) 790–796.
[25] S. Hettler, E. Kano, M. Dries, D. Gerthsen, L. Pfaffmann, M. Bruns, M. Beleggia, M. Malac, Charging of carbon thin films in scanning and phase-plate transmission electron microscopy, Ultramicroscopy 184 (2018) 252–266.
[26] C.J. Russo, R. Henderson, Charge accumulation in electron cryomicroscopy, Ultramicroscopy 187 (2018) 43–49.
[27] J. Fijol, A. Then, G. Tasker, R. Soave, Secondary electron yield of SiO2 and Si3N4 thin films for continuous dynode electron multipliers, Appl. Surf. Sci. 48 (1991) 464–471.
[28] E.R.B. Adamson, Secondary Electron Emission Coefficient From Lexan: The Low-Energy Crossover, Texas Tech University, 1993.
[29] T.J. Woehl, J.E. Evans, I. Arslan, W.D. Ristenpart, N.D. Browning, Direct in situ determination of the mechanisms controlling nanoparticle nucleation and growth, ACS Nano 6 (2012) 8599–8610.
[30] N.D. Loh, S. Sen, M. Bosman, S.F. Tan, J. Zhong, C.A. Nijhuis, P. Kral, P. Matsudaira, U. Mirsaidov, Multistep nucleation of nanocrystals in aqueous solution, Nat. Chem. 9 (2017) 77–82.
[31] E. Gachard, H. Remita, J. Khatouri, B. Keita, L. Nadjo, J. Belloni, Radiation-induced and chemical formation of gold clusters, New J. Chem. 22 (1998) 1257–1265.
[32] M. Wang, C. Park, T.J. Woehl, Quantifying the nucleation and growth kinetics of electron beam nanochemistry with liquid cell scanning transmission electron microscopy, Chem. Mater. 30 (2018) 7727–7736.
[33] C. Zhu, S. Liang, E. Song, Y. Zhou, W. Wang, F. Shan, Y. Shi, C. Hao, K. Yin, T. Zhang, et al., In-situ liquid cell transmission electron microscopy investigation on oriented attachment of gold nanoparticles, Nat. Commun. 9 (2018) 1–7.
[34] W. Wei, H. Zhang, W. Wang, M. Dong, M. Nie, L. Sun, F. Xu, Observing the growth of Pb3O4 nanocrystals by in situ liquid cell transmission electron microscopy, ACS Appl. Mater. Interfaces 11 (2019) 24478–24484.
[35] A. Ren, D. Lu, E. Wong, M.R. Hauwiller, A.P. Alivisatos, G. Ren, Real-time observation of dynamic structure of liquid-vapor interface at nanometer resolution in electron irradiated sodium chloride crystals, Sci. Rep. 10 (2020) 1–13.
[36] K. Lim, Y. Bae, S. Jeon, K. Kim, B.H. Kim, J. Kim, S. Kang, T. Heo, J. Park, W.C. Lee, A large-scale array of ordered graphene-sandwiched chambers for quantitative liquid-phase transmission electron microscopy, Adv. Mater. 32 (2020), 2002889.
[37] H.A. Schwarz, Applications of the spur diffusion model to the radiation chemistry of aqueous solutions, J. Phys. Chem. 73 (1969) 1928–1937.
[38] J.M. Grogan, N.M. Schneider, F.M. Ross, H.H. Bau, Bubble and pattern formation in liquid induced by an electron beam, Nano Lett. 14 (2014) 359–364.
[39] S Le Caër, Water radiolysis: influence of oxide surfaces on H2 production under ionizing radiation, Water 3 (2011) 235–253.
[40] T. Woehl, P. Abellan, Defining the radiation chemistry during liquid cell electron microscopy to enable visualization of nanomaterial growth and degradation dynamics, J. Microsc. 265 (2017) 135–147.
[41] J. Yang, C.M. Andrei, G.A. Botton, L. Soleymani, In liquid observation and quantification of nucleation and growth of gold nanostructures using in situ transmission electron microscopy, J. Phys. Chem. C 121 (2017) 7435–7441.
[42] W.-G. Jung, J.H. Park, Y.-R. Jo, B.-J. Kim, Growth kinetics of individual Au spiky nanoparticles using liquid-cell transmission electron microscopy, J. Am. Chem. Soc. 141 (2019) 12601–12609.
[43] Y. Zhang, D. Keller, M.D. Rossell, R. Erni, Formation of Au nanoparticles in liquid cell transmission electron microscopy: from a systematic study to engineered nanostructures, Chem. Mater. 29 (2017) 10518–10525.
[44] S.-T. Wang, Y. Lin, M.H. Nielsen, C.Y. Song, M.R. Thomas, C.D. Spicer, R. Kröger, P. Ercius, S. Aloni, M.M. Stevens, Shape-controlled synthesis and in situ characterisation of anisotropic Au nanomaterials using liquid cell transmission electron microscopy, Nanoscale 11 (2019) 16801–16809.
[45] J. Scholtz, D. Dijkkamp, R. Schmitz, Secondary electron emission properties, Philips J. Res. 50 (1996) 375–389.
[46] N. Jiang, Beam damage by the induced electric field in transmission electron microscopy, Micron 83 (2016) 79–92.
[47] S. Hettler, J. Onoda, R. Wolkow, J. Pitters, M. Malac, Charging of electron beam irradiated amorphous carbon thin films at liquid nitrogen temperature, Ultramicroscopy 196 (2019) 161–166.
[48] K. Danov, R. Danev, K. Nagayama, Reconstruction of the electric charge density in thin films from the contrast transfer function measurements, Ultramicroscopy 90 (2002) 85–95.
[49] K. Danov, R. Danev, K. Nagayama, Electric charging of thin films measured using the contrast transfer function, Ultramicroscopy 87 (2001) 45–54.
[50] M. Malac, M. Beleggia, M. Kawasaki, P. Li, R.F. Egerton, Convenient contrast enhancement by a hole-free phase plate, Ultramicroscopy 118 (2012) 77–89.
[51] G.-B. Feng, M. Cao, L.-P. Yan, H.-B. Zhang, Combined effects of sample parameters on polymer charging due to electron irradiation: a contour simulation, Micron 52 (2013) 62–66.
[52] S.F. Tan, S.W. Chee, G. Lin, U. Mirsaidov, Direct observation of interactions between nanoparticles and nanoparticle self-assembly in solution, Acc. Chem. Res. 50 (2017) 1303–1312.
[53] B. Mehdi, A. Stevens, L. Kovarik, N. Jiang, H. Mehta, A. Liyu, S. Reehl, B. Stanfill, L. Luzi, W. Hao, et al., Controlling the spatio-temporal dose distribution during STEM imaging by subsampled acquisition: in-situ observations of kinetic processes in liquids, Appl. Phys. Lett. 115 (2019), 063102.
[54] Z. Wang, A.C. Bovik, Mean squared error: Love it or leave it? A new look at signal fidelity measures, IEEE Signal Process. Mag. 26 (2009) 98–117.
[55] Z. Wang, A.C. Bovik, H.R. Sheikh, E.P. Simoncelli, Image quality assessment: from error visibility to structural similarity, IEEE Trans. Image Process. 13 (2004) 600–612.
[56] P. Abellan, T. Woehl, L. Parent, N. Browning, J. Evans, I. Arslan, Factors influencing quantitative liquid (scanning) transmission electron microscopy, Chem. Commun. 50 (2014) 4873–4880.
[57] J.P. Patterson, P. Abellan, M.S. Denny Jr, C. Park, N.D. Browning, S.M. Cohen, J. E. Evans, N.C. Gianneschi, Observing the growth of metal–organic frameworks by in situ liquid cell transmission electron microscopy, J. Am. Chem. Soc. 137 (2015) 7322–7328.
[58] G. Both, E. Kanter, Z. Vager, B. Zabransky, D. Zajfman, Ultrathin foils for Coulomb-explosion experiments, Rev. Sci. Instrum. 58 (1987) 424–427.
[59] Custom Feature Detection: Bubble Tracking in 2D foams, howpublished = http://soft-matter.github.io/trackpy/v0.3.0/tutorial/custom-feature-detection.html, note = Accessed: 2010-09-30.
[60] S.M. Sze, Current transport and maximum dielectric strength of silicon nitride films, J. Appl. Phys. 38 (1967) 2951.
[61] Download Area for Poisson Superfish. https://laacg.lanl.gov/laacg/services/download_sf.phtml#ps6, Accessed: 2022-01-21.
[62] Astra. https://www.desy.de/~mpyflo/, Accessed: 2022-01-21.